



Automatic characterization of spherical metal powders by microscope image analysis: a parallel computing approach

Xiang Li¹ · Linyi Cui² · Sara Shonkwiler¹ · Sara McMains¹

Received: 12 September 2022 / Revised: 22 December 2022 / Accepted: 26 December 2022 / Published online: 18 February 2023
© The Author(s) 2023

Abstract

The microstructural characteristics of spherical metal powders play an important role in determining the quality of mechanical parts manufactured by powder metallurgy processes. Identifying the individual powder particles from their microscopic images is one of the most convenient and cost-efficient methods for the analysis of powder characteristics. Although numerous image processing algorithms have been developed for automating the powder particle identification process, they perform less accurately in identifying adjacent particles that are heavily overlapped in their image regions. We propose an automatic algorithm to robustly and accurately identify spherical powder particles, especially heavily overlapped particles, from their microscope images. A parallel computing framework is designed to further enhance the computational efficiency of the proposed algorithm. Powder characteristics such as particle size distribution and the location of potential satellite particles have been derived from our identification results. The accuracy and efficiency of our algorithm are validated by real-world scanning electron microscope images, outperforming other existing methods and achieving both precision and recall above 99%.

Keywords Microstructure characterization · Image processing · Parallel computing · Powder metallurgy

1 Introduction

In powder metallurgy processes, the microstructural characteristics of feedstock metal powders play an important role in determining final product quality. Powder characteristics such as particle morphology and size distribution greatly influence a powder's flowability and apparent density [1, 2], which subsequently impact mechanical properties, surface roughness, and/or the porosity defect level [3–5] of the final manufactured part.

As one of the primary methods for the microstructure characterization of metallic powders, scanning electron microscopy (SEM) generates high-resolution images for close-up observation of powder particles [6]. From such SEM images, powder characteristics can be qualitatively

estimated by manual interpretation [7] or quantitatively calculated by image processing techniques.

Compared to manual interpretation, automatic or semi-automatic image processing tools have proven their superior efficiency and robustness for microstructure characterization of numerous materials [8–10]. For the characterization of metal powders, existing image processing methods [11–13] focus on the recognition of individual powder particles, which can be applied to determine other essential powder characteristics such as the particle morphology and size distribution. These methods can be categorized into three approaches: the watershed segmentation approach, the circle detection approach, and the data-driven approach.

The watershed segmentation approach is widely adopted and implemented in image processing software such as ImageJ [11] and MIPAR [12]. It is able to detect individual powder particles by partitioning the input SEM image into corresponding particle regions. However, watershed segmentation usually encounters over-segmentation problems [14], and furthermore it is less accurate in recognizing powder particles that are heavily overlapped in their image

✉ Sara McMains
mcmains@berkeley.edu

¹ University of California, Berkeley, Berkeley, CA 94720, USA

² The Hong Kong Polytechnic University, Hong Kong, China

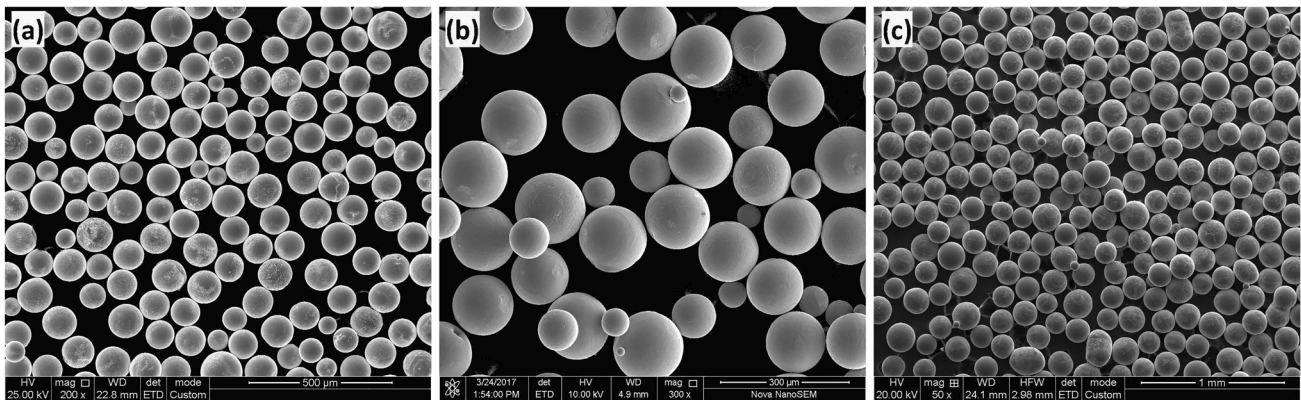


Fig. 1 Example test SEM images. **a** Ni₃Al; **b** TC4; **c** TiAl powders

regions. One example of the necessity in powder morphology of recognizing heavily overlapped powder particles is to identify the presence of “satellites”, where small “satellite” particles adhere to larger powder particles. The presence of satellite particles impedes powder flowability and subsequently leads to more internal defects in parts manufactured by powder metallurgy processes [5]. For the characterization of metal powders, accurately recognizing the heavily overlapped particles is required for high-precision analyses of particle size distribution and potential satellite locations.

On the other hand, the circle detection approach, based on algorithms such as the circular Hough transform (CHT) [13], is able to accurately identify both regular and heavily overlapped powder particles in general by recognizing their circular contours. However, in addition to being less efficient in terms of both computation time and memory requirements, this approach is prone to generate false positive detections because of its sensitivity to image noise [15].

Recently, data-driven approaches have demonstrated great potential for the quantification of metal powder particles (satellites in particular) by implementing instance segmentation and deep learning models [16, 17]. The performance of deep learning models largely depends on the quality and amount of labeled data. Because of the challenge of collecting and labeling enough representative data for the target problem, deep learning models in engineering applications generally encounter pitfalls in their applicability and reproducibility [18]. Robust rule-based powder particle identification/labeling algorithms can further improve the effectiveness of data-driven methods, for example by providing more labeled training data for deep learning.

Therefore, in this research, we propose an automatic algorithm to characterize spherical metal powders from their SEM images. Our algorithm is able to robustly identify the sizes and locations of individual powder

particles, including heavily overlapped particles. To further enhance the computational efficiency, a parallel computing framework is designed and implemented for the algorithm. The accuracy and efficiency of the proposed algorithm are validated on 50 real-world SEM images of spherical metal alloy powders.

2 Materials and methods

2.1 Materials and microscope images

For the evaluation of our algorithm, 50 SEM images were collected from three spherical metal alloy powders commonly used in powder metallurgy processes: Ni₃Al, TC4 (Ti6Al4V), and TiAl powders. The powders were first pre-alloyed and then produced by the plasma rotating electrode process, which provides powder particles with a high degree of sphericity, high flowability, and low porosity compared to other metal powder manufacturing methods [19].

The images, with resolution 1024 × 943 pixels, were taken using a Nova NanoSEMTM scanning electron microscope. Example test images are shown in Fig. 1.

2.2 Algorithm details

In order to achieve better performance in terms of both accuracy and efficiency than existing algorithms, our algorithm is designed as a three-stage scheme:

1. We first roughly partition the input SEM image into small image regions that represent individual powder particles using watershed segmentation. Heavily overlapped particles may not be correctly segmented in this stage (but will be handled in the next stage).
2. For each image region, we perform a CHT to conduct a thorough detection of powder particles (especially

overlapped particles), and then determine their exact sizes and locations. In this stage, the small-size image regions enable the CHT to significantly improve its accuracy and efficiency compared to being directly applied on the entire SEM image.

3. We collect detection results from each of the image regions and sort them into a list of detected powder particles for the entire input SEM image.

Since spherical powders are the most frequently used and in-demand type of powders in powder metallurgy processes because of their high shape consistency and superior flowability [20], we focus on the identification of metal powder particles that have a high degree of sphericity. Irregularly shaped powder particles are identified by the circular regions that best fit their contours.

2.2.1 First stage: individual particle region segmentation

In the first stage of our algorithm, using distance-transform-based watershed segmentation, we partition the input SEM image into sub-regions representing individual powder particles.

From the input SEM image (Fig. 2a), we first convert it to grayscale and then utilize a Gaussian filter to eliminate high-frequency image noise. Otsu's method [21] for automatic image thresholding is then applied to convert the grayscale image into a binary image (Fig. 2b) by separating its image pixels into two classes based on their pixel intensity: the (lighter) powder particle pixels and the

(darker) background pixels. Next, to remove the remaining image noise or microstructural artifacts (e.g., debris from broken particles), morphological operations such as opening and area opening [22] are applied on the binary image.

Next, we implement distance-transform-based watershed segmentation [23] to recognize image regions corresponding to individual powder particles. This method constructs the distance transform of our denoised, thresholded binary image (Fig. 2c) and applies watershed segmentation to it (Fig. 2d). We also adopt our over-segmentation detection and merging method [14] as a post-processing step to address the impact of over-segmentation, which is otherwise typically one of the shortcomings of watershed segmentation.

This watershed segmentation stage works well on segmenting image regions of isolated or slightly overlapped powder particles. However, this process is less effective on segmenting heavily overlapped powder particles because they are not easily distinguishable from each other in binary images. Furthermore, instead of exact sizes and locations of powder particles, the watershed segmentation only provides their segmented image regions, which cannot be directly used to quantify powder characteristics like the particle size distribution. Hence, the second stage of our algorithm is designed to address the aforementioned problems.

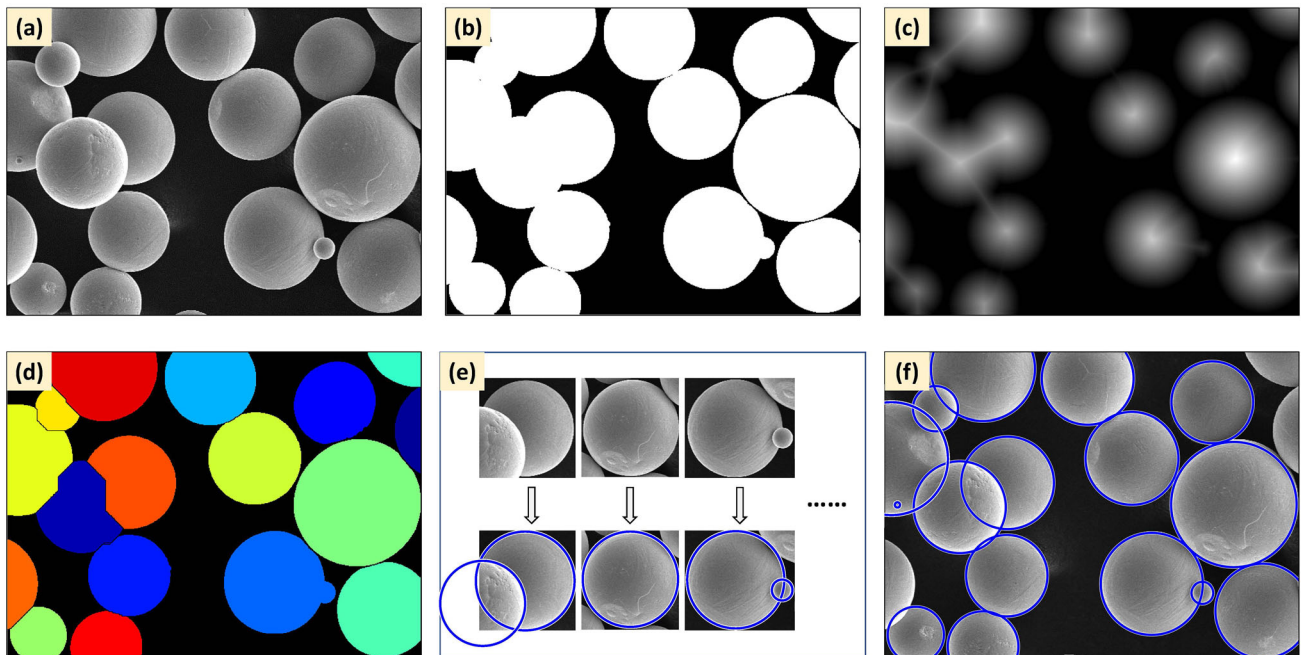


Fig. 2 Algorithm overview. **a** Input SEM image; **b** image thresholding and noise reduction; **c** distance transform; **d** individual particle region segmentation; **e** circular Hough transform in each image region; **f** identified powder particles after result summarizing across image regions

2.2.2 Second stage: circle detection in each image region

In the second stage of our algorithm, in order to determine the exact sizes and locations of spherical particles and the existence of heavily overlapped particles, we conduct a circle detection process on the input SEM image, inside each of the corresponding image regions calculated from the first stage.

The circular Hough transform [13] is applied in this stage for the detection of spherical powder particles. As shown in Fig. 3, in each image region, individual powder particles, including heavily overlapped particles, are detected as circles by the algorithm. Their sizes and relative locations in the corresponding image regions (as distinguished from their “global” locations in the entire input image, which will be calculated in the third stage) are also determined. Note that a powder particle might be detected in more than one image region if it overlaps with other particles.

The accuracy and efficiency of the circular Hough transform directly relate to the size of the target image region. Smaller image regions lead to a more accurate and efficient circle detection process. By reducing the target image region from the entire SEM image to individual particle regions, our algorithm significantly improves both the accuracy and efficiency of the identification of

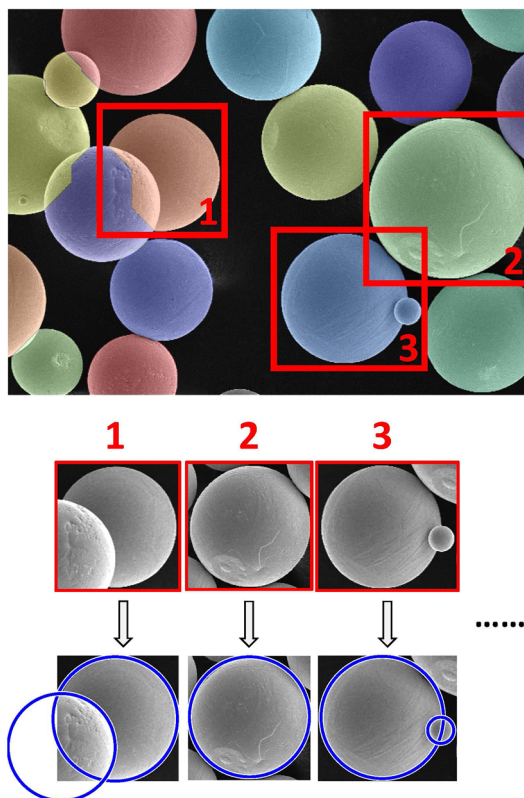


Fig. 3 Representative examples of circle detection results

spherical powder particles compared to existing methods (see Sect. 3).

2.2.3 Third stage: result sorting across image regions

In the final stage of our algorithm, we collect circle detection results from each image region and sort them into a list of detected powder particles for the entire input SEM image (Fig. 2f). In this sorting process, the relative “local” locations of detected particles from each image region are converted into their “global” locations in the (entire) input image. Since overlapped powder particles might be contained in multiple image regions, we identify and eliminate such repeated detections by checking identified powder particles with similar radii and global locations.

2.3 Parallel computing framework

The second stage of our algorithm is well-suited for parallel computing, wherein larger, complex problems are broken into smaller, independent tasks that can be executed simultaneously [24]. The implementation of CHT algorithm in each segmented image region is an independent task and does not impact the computation process or result for any other image regions. Since an input SEM image may contain as many as hundreds of powder particles, parallelizing the second stage of our algorithm (CHT computations in each of the corresponding particle regions) can significantly reduce the overall computation time (see Sect. 3.3).

Therefore, we design a parallel computing framework for the proposed algorithm. As illustrated in Fig. 4, the second stage (circle detection) is implemented in parallel on the graphics processing unit (GPU) by simultaneously conducting circle detection (CHT) computation in each of the image regions. Other parts of the algorithm (the first and third stages) are still implemented in serial on the central processing unit (CPU).

3 Results and discussion

3.1 Overview

Our algorithm has been implemented in MATLAB (serial computing stages) and CUDA/C++ (parallel computing stages), and run on a PC with an Intel Core™ Processor i7-8550U CPU with 16 GB RAM and an NVIDIA GeForce GTX 1080 Ti graphics card.

The ground truth powder identification results were manually determined by two powder metallurgy experts independently. They had consistent classifications of the

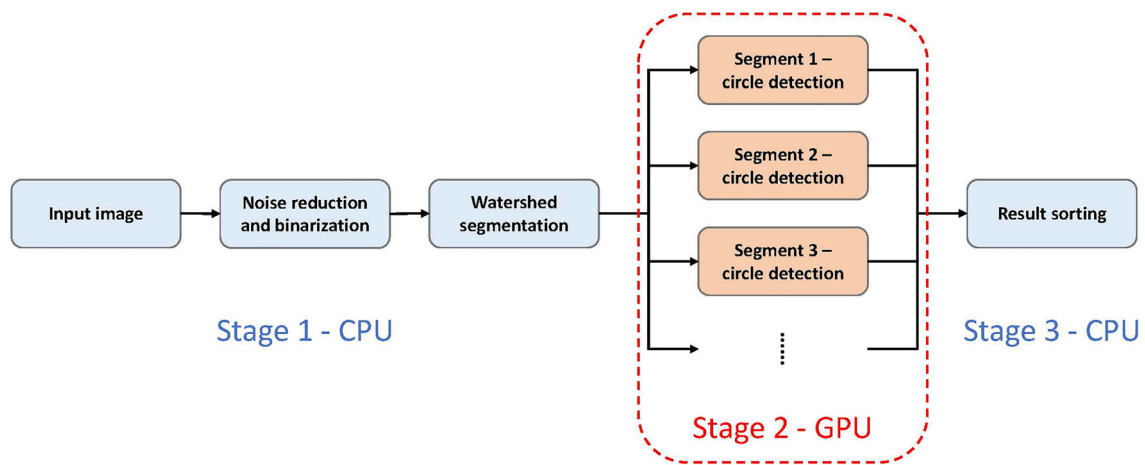


Fig. 4 Parallel computing framework of our algorithm

locations and sizes of all powder particles across our 50 test SEM images (as described in Sect. 2.1).

For comparison with our algorithm, we implemented two existing methods, watershed segmentation and the CHT, and then tested them on our SEM images. Since watershed segmentation is only able to provide image regions representing individual powder particles but not their exact sizes and locations, a least-squares fitting technique [25] was applied on each segmented image region as a post-processing step for the watershed method, for accurate identification of particle sizes and locations.

We validated our algorithm on the 50 test SEM images. As shown in Fig. 5, from the test images, our proposed algorithm successfully identified individual spherical powder particles no matter whether they were heavily overlapped or not. It outperformed existing algorithms in both accuracy and efficiency. In the rest of this section, we present detailed analyses of the accuracy (Sect. 3.2) and efficiency (Sect. 3.3) of our algorithm and (in Sect. 3.4) discuss how the identification results can be further applied in determining powder characteristics such as particle size distribution and potential satellite positions.

3.2 Accuracy

In our experiments, the identification results of individual powder particles can be classified into three types:

- True positive (TP): real powder particle positions that are correctly identified.
- False negative (FN): real powder particle positions that are not identified.
- False positive (FP): non-powder-particle positions that are misidentified as powder particles.

Precision and recall metrics are calculated to quantitatively compare the accuracy of our proposed algorithm to

other existing methods. In this context, precision is the probability that identified powder particles are real powder particles, whereas recall is the probability that real powder particles are successfully identified by the algorithm. Mathematically, these two metrics can be expressed as follows:

$$\text{Precision} = \frac{\text{TP}}{\text{TP} + \text{FP}} \quad (1)$$

$$\text{Recall} = \frac{\text{TP}}{\text{TP} + \text{FN}} \quad (2)$$

Note that there is a tradeoff between precision and recall for the CHT algorithm. Thus, we chose to tune its user-defined parameters (e.g., voting sensitivity) to minimize the total number of false positives and false negatives. For example, as shown with the two different CHT results pictured in Fig. 5, while determining the optimal parameter values for the CHT method, the lower sensitivity was ultimately selected because it led to the fewest total mistakes (5 false negatives) compared to other parameter values, such as the second best sensitivity choice (high sensitivity in Fig. 5) that resulted in 6 mistakes (4 false negatives + 2 false positives).

Table 1 summarizes the overall precision and recall of our proposed algorithm and the two existing comparison methods across the 50 test images. The watershed segmentation performed well on the identification precision (99.3%), but had a low recall value (89.2%) due to its inability to identify heavily overlapped powder particles, which leads to false negatives (particles not detected). The CHT method is sensitive to image noise and usually performs poorly on detecting circles with a wide range of size variation. For powder particle identification with the CHT method, the aforementioned problems give rise to both false positives and false negatives and subsequently

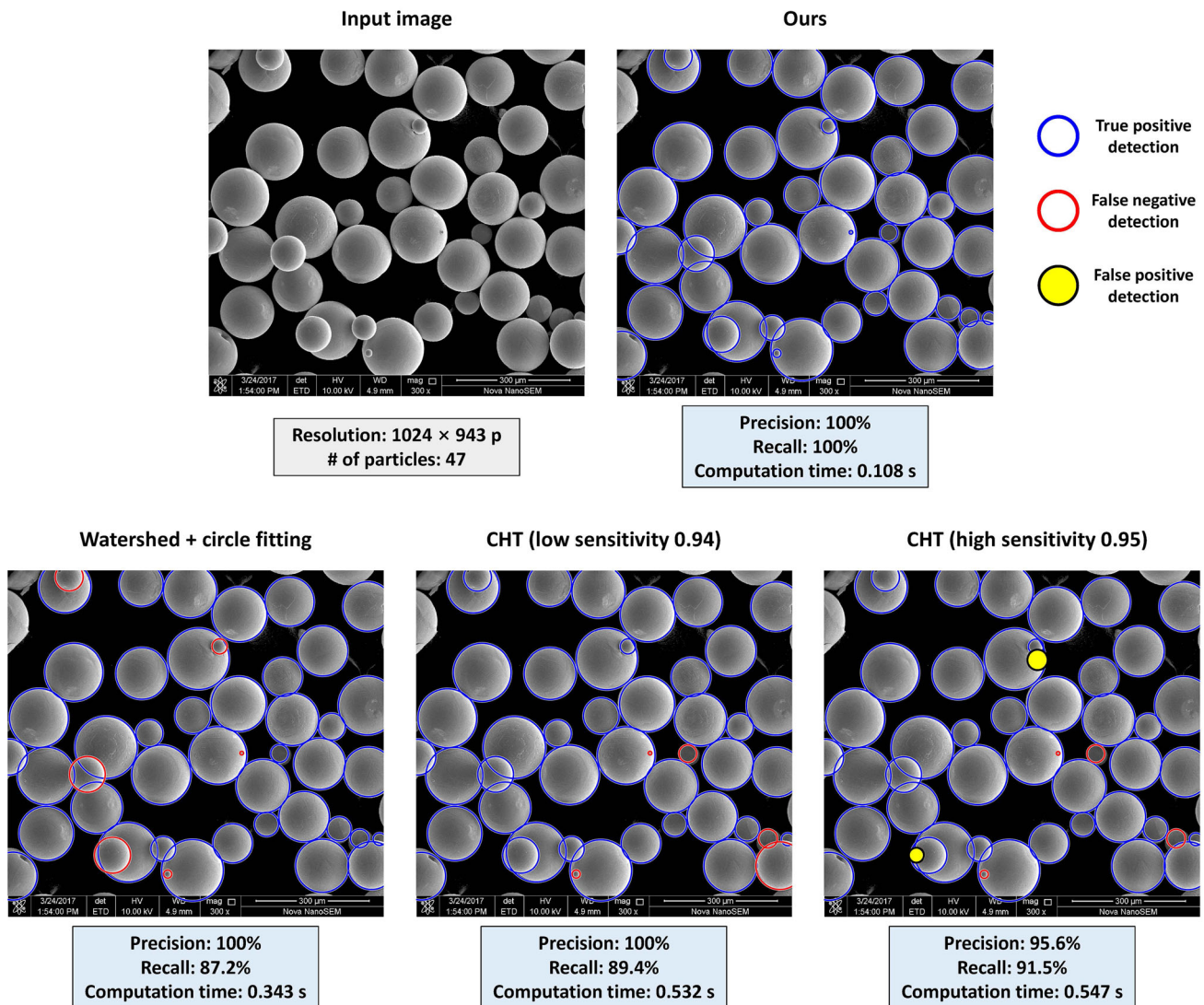


Fig. 5 Experimental result comparison between our proposed algorithm and other existing methods

Table 1 Accuracy comparison between our proposed algorithm and other existing methods (%)

Algorithm	Ours	Watershed	CHT
Precision	99.3	99.3	95.2
Recall	99.5	89.2	93.8

influence the method's precision and recall values (95.2% and 93.8%, respectively).

Our proposed algorithm achieved the best performance in both precision and recall. In our algorithm, the individual particle region segmentation eliminates the vast majority of image noise and artifacts and narrows down the region of interest from the entire SEM image to small image regions representing individual powder particles.

Consequently, by implementing the CHT algorithm in each of these small segmented image regions, our circle detection stage demonstrated excellent robustness and accuracy, leading to 99.3% precision and 99.5% recall rates in the identification of individual powder particles.

3.3 Efficiency

The manual labeling of powder particles is an accurate but time consuming process. Automatic image processing algorithms are orders of magnitude faster than the manual labeling process, even performed by experienced material experts. Among these automatic algorithms, as well as obtaining the best accuracy, our proposed algorithm also required the least computation time, with the comparison algorithms taking about 3–5 times longer (Table 2), though all took less than 1 s.

Table 2 Efficiency comparison between our proposed algorithm and existing automatic methods (computation time per SEM image)

Ours	Watershed	CHT
0.136 s	0.365 s	0.688 s

It is computationally expensive to directly analyze high-resolution SEM images by the CHT method since its computational complexity has a quadratic relationship to the size (number of pixels) of the input image [26]. On the other hand, although watershed segmentation is efficient for segmenting particle regions, it requires a subsequent circle fitting post-process for particle size and location determination, which substantially increases the overall computation time of the watershed method.

Due to the effectiveness of our three-stage powder identification procedure and parallel computing framework, our algorithm reduced the computation time by 63% and 80% compared to the watershed and the CHT methods.

3.4 Powder characteristics

The accurate identification of powder particles enables us to further derive various powder characteristics, such as particle size distributions and the position of those particles identified as potential satellites.

Note that the classification of satellite particles, those small powder particles that physically adhere to larger powder particles, cannot be definitively determined from SEM images since often only the geometric overlapping relations among powder particles can be observed from 2D images, but not their physical connections. However, from

our identification results, we are able to provide potential positions that have a high probability of being satellites.

We mathematically define potential satellite particles as follows: those identified particles that a) have their centers located inside at least one other particle (an overlapping particle), and b) the satellite particle has smaller diameter than (one of) its overlapping particle(s). As shown in Fig. 6b, following our definition, potential satellite positions are calculated and highlighted. Such potential satellite positions can then be used to assist researchers to further interpret/predict powder characteristics such as the level of agglomeration and powder flowability [5].

From the particle identification results, the particle size distribution can also be derived and represented in either the form of a histogram (Fig. 6c) or percentile values of identified powder particles' diameters.

4 Conclusion

In this paper, we have presented an automatic algorithm to identify spherical metal powder particles from SEM images. The novel three-stage procedure and parallel computing architecture enable our algorithm to outperform other existing methods in both accuracy and efficiency. The algorithm successfully handles all 50 test SEM images, robustly identifies powder particles, and calculates their exact locations and sizes. It achieves an overall precision and recall of 99.3% and 99.5%, respectively, and an average computation time of 0.136 s per SEM image. From the identification results, powder characteristics such as particle size distribution and potential satellite positions are also quantified and visualized for researchers to further investigate powder properties.

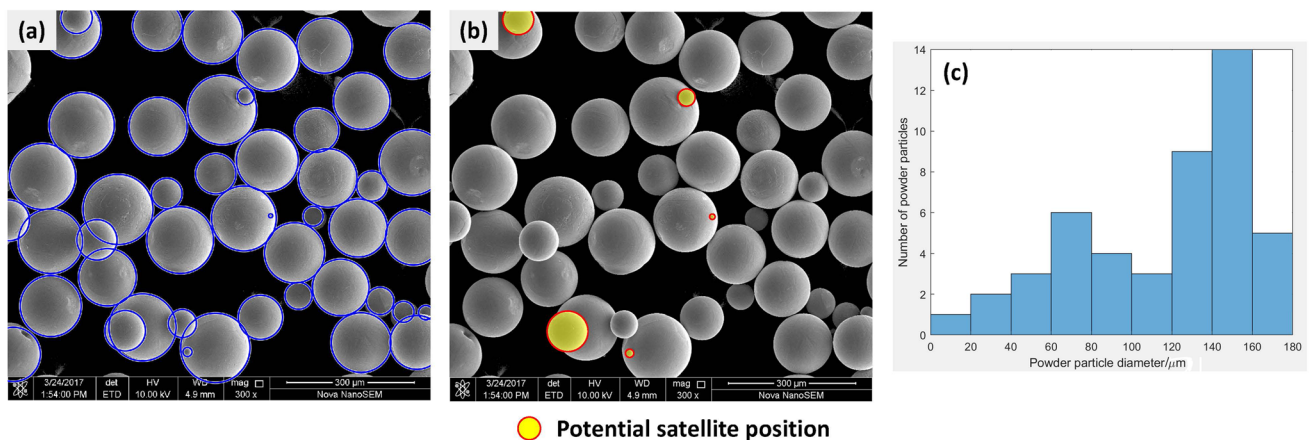


Fig. 6 An example of our identification results and its derived powder characteristics (a), potential satellite positions (b), and particle size distribution (c)

Acknowledgements We gratefully acknowledge Lin Zhao for providing test SEM images and material experts from China Iron and Steel Research Institute Group for generating the ground truth labels.

Declarations

Conflict of interest The authors declare that they have no known competing financial interests or personal relationships that could have appeared to influence the work reported in this paper.

Open Access This article is licensed under a Creative Commons Attribution 4.0 International License, which permits use, sharing, adaptation, distribution and reproduction in any medium or format, as long as you give appropriate credit to the original author(s) and the source, provide a link to the Creative Commons licence, and indicate if changes were made. The images or other third party material in this article are included in the article's Creative Commons licence, unless indicated otherwise in a credit line to the material. If material is not included in the article's Creative Commons licence and your intended use is not permitted by statutory regulation or exceeds the permitted use, you will need to obtain permission directly from the copyright holder. To view a copy of this licence, visit <http://creativecommons.org/licenses/by/4.0/>.

References

- [1] M.A. Spurek, L. Haferkamp, C. Weiss, A.B. Spierings, J.H. Schleifenbaum, K. Wegener, *Prog. Addit. Manuf.* 7 (2022) 533–542.
- [2] P. Kiani, U. Scipioni Bertoli, A.D. Dupuy, K. Ma, J.M. Schoenung, *Adv. Eng. Mater.* 22 (2020) 2000022.
- [3] C. Pleass, S. Jothi, *Addit. Manuf.* 24 (2018) 419–431.
- [4] S.E. Brika, M. Letenneur, C.A. Dion, V. Brailovski, *Addit. Manuf.* 31 (2020) 100929.
- [5] F. Chu, K. Zhang, H. Shen, M. Liu, W. Huang, X. Zhang, E. Liang, Z. Zhou, L. Lei, J. Hou, A. Huang, *J. Mater. Res. Technol.* 11 (2021) 2059–2073.
- [6] J.A. Slotwinski, E.J. Garboczi, P.E. Stutzman, C.F. Ferraris, S.S. Watson, M.A. Peltz, *J. Res. Natl. Inst. Stand. Technol.* 119 (2014) 460–493.
- [7] L.W. Hunter, D. Brackett, N. Brierley, J. Yang, M.M. Attallah, *Int. J. Adv. Manuf. Technol.* 106 (2020) 4521–4532.
- [8] X. Li, S. Shonkwiler, S. McMains, *Compos. Part B Eng.* 225 (2021) 109252.
- [9] C. Barbosa, J.B. De Campos, J.L. do Nascimento, I.M.V. Caminha, *J. Iron Steel Res. Int.* 16 (2009) 18–21.
- [10] X. Li, L. Cui, J. Li, Y. Chen, W. Han, S. Shonkwiler, S. McMains, *Mater. Des.* 224 (2022) 111358.
- [11] C.A. Schneider, W.S. Rasband, K.W. Eliceiri, *Nat. Methods* 9 (2012) 671–675.
- [12] J.M. Sosa, D.E. Huber, B. Welk, H.L. Fraser, *Integr. Mater. Manuf. Innov.* 3 (2014) 123–140.
- [13] T.J. Atherton, D.J. Kerbyson, *Image Vision Comput.* 17 (1999) 795–803.
- [14] X. Li, S. Shonkwiler, S. McMains, in: 2021 IEEE International Conference on Image Processing (ICIP), Anchorage, USA, 2021, pp. 2623–2627.
- [15] P. Mukhopadhyay, B.B. Chaudhuri, *Pattern Recogn.* 48 (2015) 993–1010.
- [16] S.E. Price, M.A. Gleason, B.C. Sousa, D.L. Cote, R. Neamtu, *Integr. Mater. Manuf. Innov.* 10 (2021) 661–676.
- [17] R. Cohn, I. Anderson, T. Prost, J. Tiarks, E. White, E. Holm, *JOM* 73 (2021) 2159–2172.
- [18] M. Roberts, D. Driggs, M. Thorpe, J. Gilbey, M. Yeung, S. Ursprung, A.I. Aviles-Rivero, C. Etmann, C. McCague, L. Beer, J.R. Weir-McCall, Z. Teng, E. Gkrania-Klotasa, AIX-COVNET, J.H.F. Rudd, E. Sala, C.B. Schonlieb, *Nat. Mach. Intell.* 3 (2021) 199–217.
- [19] P. Moghimian, T. Poirie, M. Habibnejad-Korayem, J.A. Zavala, J. Kroeger, F. Marion, F. Larouche, *Addit. Manuf.* 43 (2021) 102017.
- [20] Q. Bao, Y. Yang, X. Wen, L. Guo, Z. Guo, *Mater. Des.* 199 (2021) 109382.
- [21] N. Otsu, *IEEE Trans. Syst. Man Cybern.* 9 (1979) 62–66.
- [22] R.M. Haralick, L.G. Shapiro, *Computer and robot vision*, vol. 1, Addison-Wesley Reading, Boston, USA, 1992.
- [23] P. Acharjya, A. Sinha, S. Sarkar, S. Dey, S. Ghosh, *Int. J. Adv. Res. Comput. Commun. Eng.* 1 (2013) 185–189.
- [24] X. Li, A. Krishnamurthy, I. Hanniel, S. McMains, *Comput. Graph.* 82 (2019) 332–342.
- [25] V. Pratt, *ACM SIGGRAPH Comput. Graph.* 21 (1987) 145–152.
- [26] C. Hollitt, in: 2009 24th International Conference Image and Vision Computing, New Zealand, 2009, pp. 373–378.